Article:

An Evaluation of Shoe Tread Parameters using FEM

J. Hale*, A. O'Connell, R. Lewis, M.J Carré, J.A Rongong

Email: jhale1@sheffield.ac.uk

Department of Mechanical Engineering, University of Sheffield, Mappin Street, Sheffield S1 3JD, UK

Abstract

Within this paper, a three-dimensional finite element (FE) model of a uniformly loaded, single rubber block, is described and run using loading conditions replicative of a standard slip resistant footwear test. The FE model considers rubber hyperelastic and viscoelastic material properties, obtained using dynamic mechanical analysis. The performance of the FE model was evaluated through analytical compression analysis and experimental contact area testing. The effect of tread grooves was investigated with relation to slip-resistance during walking. Analysis and discussion are provided of the tread model's sliding contact areas, contact pressure, stress, and front edge mechanics.

Keywords: Rubber, Tread, Finite Element, Footwear

1. Introduction

Slip related accidents are a major cause of injury in workplaces worldwide. Within the UK alone, the Health and Safety Executive (HSE) reported that slips, trips and falls, onto the same level, are the highest cause of non-fatal injuries, accounting for 29% of all reported non-fatal work injuries in 2018/19 [1].

Figure 1. Anvil Traction Shoe (left) and tread orientation definitions (right). The arrows indicate the slide direction.

To reduce the likelihood of a slip occurring, slip resistant footwear can be worn [2]. An example is shown in Figure 1. Such footwear typically has a rubber outsole with numerous tread elements, and consequent grooves or sipes. Thus, via discrete areas of high pressure caused by tread elements, and the presence of fluid channels, surface fluids and contaminants can be effectively dispersed. This prevents the formulation of a fluid film, ensuring dry shoe-surface contact [3]. If a fluid film is present between the shoe outsole and the ground, friction is reduced by orders of magnitude due to hydrodynamic effects.

The frictional performance of slip resistant footwear has been extensively studied experimentally [4–9]. Two studies by Li and Chin (2004) and Li and Chen (2005), investigated how certain tread design parameters affect friction on contaminated surfaces using bespoke tread patterns [4,5]. It was observed that tread orientated perpendicular or oblique to the slide direction produced a higher dynamic friction coefficient (μ_k) than tread orientated parallel to the slide direction (Figure 1) [5]. Furthermore, by comparing the performance of treads with 3 and 9 mm grooves, it was determined that wider tread grooves produced higher μ_k [4]. Both these findings have been supported by Blanchette and Powers [9] who comment that the perpendicular tread provides good resistance to motion but poor liquid dispersion while an oblique pattern is capable of both and is therefore preferred. Although these experimental investigations provide invaluable insights into how shoe tread parameters influence μ_k, custom built outsoles were manufactured to do so. This sacrifices the validity of the observed results when comparing to real, complex outsole designs, as shown in Figure 1.

The Finite Element Method (FEM) allows evaluation of real tread designs, while providing detailed stress and strain information that cannot be easily obtained experimentally. Consequently, it has been frequently utilised to examine rubber sliding scenarios [8,10–12]. A notable FEM study is that by Hofstetter et al. (2006) on motor vehicle tyre treads, that was able to replicate the characteristic front edge curling characteristic of sliding rubber that is linked to the rubber's overall μ_k [12]. An FE model of a real shoe tread pattern, capable of detailing the leading edge pressure concentrations, would provide an understanding of how the real shoe μ_k is produced and enable investigations into the effects of design parameters such as shape and elastic modulus.

This paper details the development and initial validation of an FE model and its use to increase understanding of the frictional implications of slip resistant footwear tread patterns and material characteristics. It does this by first modelling a single tread element before analysing a tread pattern from a real slip resistant shoe.

2. Methodology

The reason for developing the FE approach for shoe tread analysis was to provide insight into the deformation of the tread under typical dynamic loading. A model with simplified geometry was used to demonstrate that the approach used is appropriate for this type of analysis. Subsequently, the behaviour of a realistic tread pattern was studied following the approach developed.

ABAQUS 2018 FE software (Dassault Systèmes, Vélizy-Villacoublay, France) was selected to conduct the planned FE analysis due to its capabilities with modelling hyperelastic and viscoelastic rubber materials as well as its competency in simulating dynamic sliding conditions [13,14].

2.1 Model Creation

2.1.1 Geometry

FE model geometries were taken directly from an Anvil Traction outsole. As Figure 2 shows, a key feature of the outsole is the presence of 6 mm × 6 mm square tread elements, comprising four identical 2.5 mm × 2.5 mm smaller squares with a 1 mm groove running between them. To reduce computational cost and convergence difficulties, the model was initially evaluated as a single 6 mm × 6 mm square block. Subsequently, the model was made more representative by the adding grooves and then replicating four times to form a tread pattern identical to the 8 mm × 8 mm repeating unit on the Anvil Traction outsole but scaled to 200%.
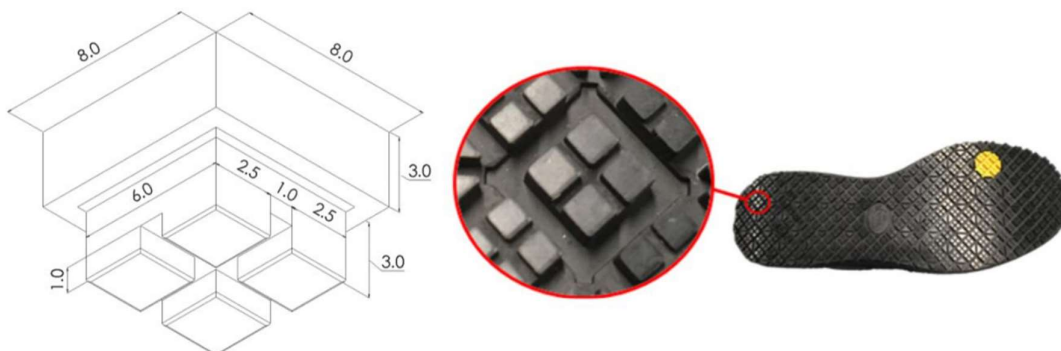
Figure 2. Tread geometry from Anvil traction shoe (dimensions in mm).

Since the structure is symmetric, simulation was run on half the geometry and then mirrored.

The contact surface was modelled as an infinitely stiff, rigid and smooth surface. Therefore, no surface mesh was necessary and computational cost was reduced, decreasing any accuracy losses in the three-dimensional contact analyses.

2.1.2 Material Properties

All material properties used in the FE model were based on a rubber (TY-Green) provided by Anvil Traction. The approach taken was to represent the material using a linear hyperelastic and viscoelastic model. This was considered reasonable because TY-Green has a relatively low filler content (with no carbon black) and the expected strain levels on the tread were not expected to be particularly high.

The neo-Hooke model was used to represent the rubber's hyperelasticity. Thus, a neo-Hookean strain energy function was used as shown in Equation 1.

$$W = C_{10}(I_1 - 3) + \frac{1}{D_1}(J_{el} - 1)^2$$

Equation 1

All the parameters in Equation 1 can be empirically determined. C_{10} controls the shear behaviour of the material, D_1 represents bulk compressibility and can be determined from the shear (G) and bulk (K) moduli, which can in turn be determined from the Young's modulus (E) and Poisson's ratio (v) as shown in Equations 2 and 3.

$$C_{10} = \frac{G}{2} = \frac{\left(\frac{E}{2(1+v)}\right)}{2}$$

Equation 2

$$D_1 = \frac{2}{K} = \frac{2}{\left(\frac{E}{3(1-2v)}\right)}$$

Equation 3

Viscoelasticity was incorporated into the FE model using the generalised Maxwell model which describes the rubber as a linear viscoelastic material, expressed as a set of Maxwell elements, each of which is formed of an elastic spring connected in series to a viscous dashpot. To represent behaviour numerically in the time domain, the relaxation modulus $E(t)$ was then defined using the Prony series shown in Equation 4.

$$E(t) = E_\infty \left[1 + \frac{\sum_{i=1}^{N} g_i e^{\frac{-t}{\tau_i}}}{1 - \sum_{i=1}^{N} g_i} \right]$$

Equation 4

where E_∞ is the long term Young's modulus, t is the elapsed time and the parameters g_i and τ_i are the ith modulus and relaxation time constants respectively.

Dynamical Mechanical Analysis (DMA) was used to obtain the properties of the TY-Green rubber studied in this work. The storage modulus (E'), loss modulus (E'') and loss factor ($tan\delta$) were obtained at several frequencies between 1 and 30 Hz over a temperature range of -40 to 50 °C. Master curves were then generated using the frequency-temperature superposition principle and a reference temperature of 20 °C. Prony series coefficients fitted to the data at the reference temperature are provided in Table 1 while the results of the curve-fit are shown in Figure 3. Note that the Prony model matches the test data well in terms of modulus but underestimates the loss factor at low frequencies. This inability to match both curves is typical of this type of fitted model because it incorporates an inbuilt expectation that the gradient of the modulus curve is linked to the absolute value of the loss factor [15]. This shows that there may be other sources of energy loss within this particular material. However, this does not detract from the suitability of the general approach.

Table 1. Prony series coefficients for TY-Green rubber with $E_\infty = 7.33$ MPa

i	g_i	τ_i	i	g_i	τ_i	i	g_i	τ_i
1	2.0847e-03	2.7384e+03	6	4.6438e-03	4.2170e-02	11	2.5698e-01	6.4938e-07
2	1.1450e-03	2.9854e+02	7	9.4109e-03	4.5973e-03	12	2.4128e-01	7.0795e-08
3	2.0380e-03	3.2546e+01	8	2.2960e-02	5.0119e-04	13	1.0928e-01	7.7179e-09
4	2.3540e-03	3.5481e+00	9	5.5435e-02	5.4639e-05	14	3.6583e-02	8.4140e-10
5	3.2522e-03	3.8681e-01	10	1.3669e-01	5.9566e-06	15	9.6349e-02	9.1728e-11

For viscoelastic materials it is known that the Poisson's ratio changes from approximately 0.5 to 0.33 as it transitions from the rubbery to the glassy state [16]. Around the reference temperature it can be seen from Figure 3 that motions taking longer than about 1 millisecond are within the rubbery zone and hence, because the bulk modulus of rubbery polymers is around 2 GPa, a Poisson's ratio of approximately 0.4994.
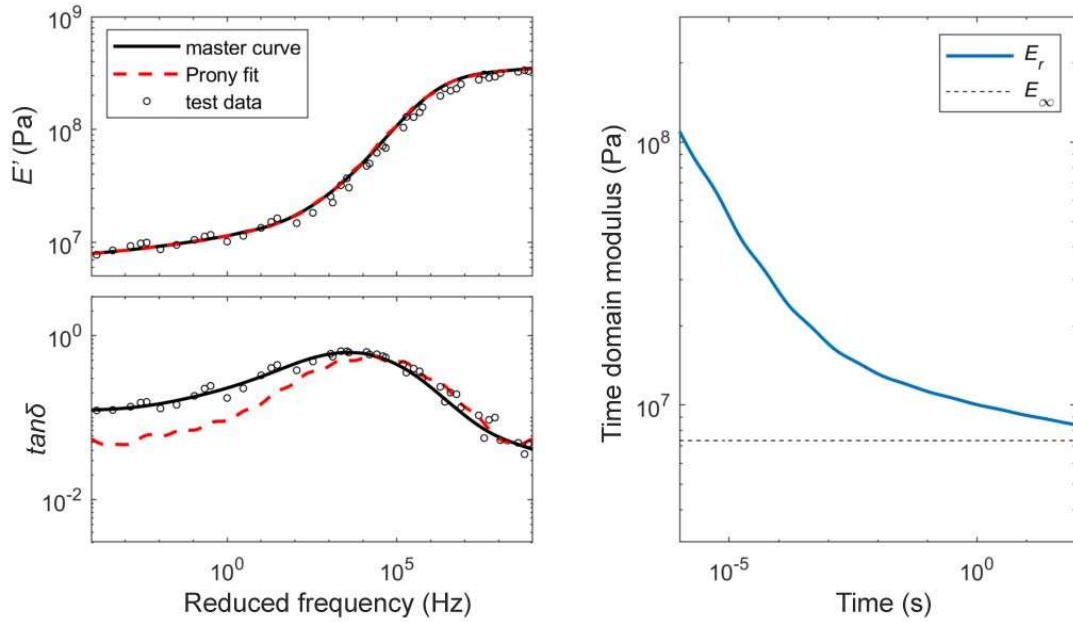
Figure 3. Frequency domain complex modulus and time domain relaxation modulus of TY-Green rubber.

2.2 Boundary Conditions

The simulation was split into two distinct steps, imitating the conditions a shoe experiences during slip testing as specified by BS EN ISO 13287:2012. The first step involved a normal load applied to the top face of the tread model, lasting 0.1 s. The second step was the application of a horizontal, constant velocity applied to the top tread surface and lasting for 0.3 s. Figure 4 illustrates these two simulation steps as applied to the model of a single tread unit.
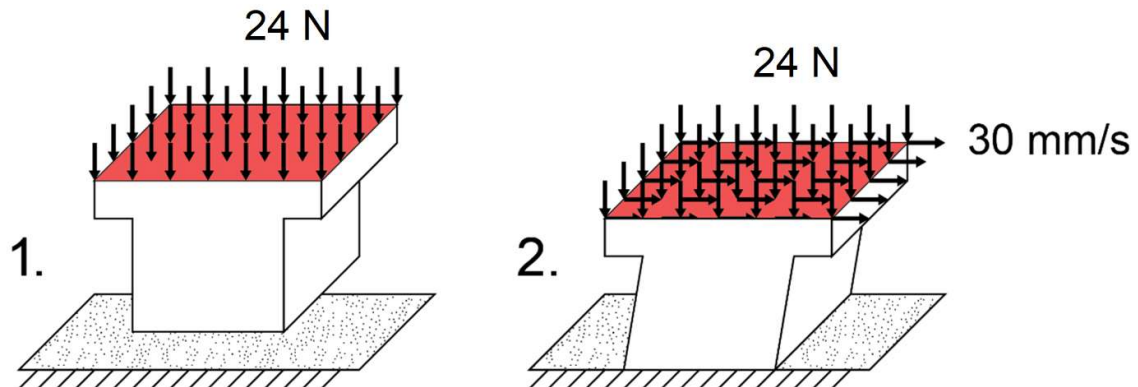
Figure 4. The two loading steps in the simulation and the applied normal load and slide velocity.

Taking the normal load applied from the aforementioned standard (500 N), it was calculated, that under typical conditions, this is equivalent to a normal load of 24 N applied as evenly

distributed pressure over the 8 mm × 8 mm repeating unit shown previously in Figure 2. Note that for the half-width, mirrored models, this therefore represented a 12 N normal load.

The friction coefficient (μ_k) between surface and tread was set to be 0.55. This value was obtained experimentally from sliding a 20 × 30 mm TY-Green rubber block across a Eurotile surface at a normal load of 200 N and slide velocity of 10 mm/s. These experiments were conducted on a Universal Mechanical Tester (UMT) (UMT TriboLab, Bruker, Massachusetts, USA). The nominal contact pressure was equal in friction experiment and FE simulation. It is acknowledged that the friction between rubber and dry surfaces is likely to change due to changes in local contact pressures, meaning the realistic tread pattern is likely to produce a different friction to that of the single block. However, for simplicity, μ_k was kept at 0.55 for the baseline analysis. The effects of reducing μ_k was explored numerically.

For all simulations, surface fluids and contaminants were not included. This means that the resulting model assumed that surface contaminants were being adequately dispersed during sliding, providing dry contact between the surface and the rubber tread. Making this assumption also drastically reduced the complexity of simulation.

2.3 Initial validation using the simplified block model

The FE model of the simplified 6 mm × 6 mm block was constructed from three-dimension first order elements with a hybrid pressure formulation and reduced integration. Note that although second order elements are typically preferred for continuous stress analysis, they are less suitable for contact problems as they can encounter convergence problems during contact due to an imbalance between compressive and tensile forces within the element. An initial mesh convergence study indicated that elements of nominal size 0.1 mm provided a reasonable trade-off between accuracy and calculation time.

Two tasks were undertaken to illustrate the suitability of the modelling approach. In the first, the deflection of the block under compression loading was compared with results from analytical expressions. In the second, the sensitivity of the results to friction coefficient and material compressibility were investigated. Lastly, the friction force and contact area over time are compared to that obtained experimentally. It is acknowledged that these tests do not comprehensively validate the model. Instead, they demonstrate that the model behaves in a reasonable and justifiable manner.

2.3.1 Compression behaviour

Comparison with analytical results was conducted considering the degree of y-displacement during the initial compression phase. Interface friction conditions of zero and infinity (i.e. bonded) were achieved by utilising Gent's shape factor approach for determining the

deflection of constrained rubber blocks [17]. In this approach, the total vertical compression of a rubber block can be determined by defining the compression spring rate (k_c) as the amount of compressive force (F_c) required to cause a unit deflection (d_c) as stated in Equation 5.

$$k_c = \frac{F_c}{d_c}$$

<div align="right">**Equation 5**</div>

Defining k_c in terms of the loaded area during compression (length l multiplied by width w), the undeformed block thickness (t) and the compression modulus (E_c) gives Equation 6.

$$k_c = \frac{lwE_c}{t}$$

<div align="right">**Equation 6**</div>

E_c can be defined as done in Equation 7,

$$E_c = E_0(1 + \psi S^2)$$

<div align="right">**Equation 7**</div>

where E_0 is the Young's modulus, ψ is a coefficient that accounts for material compressibility and cross-sectional shape and S is a geometrical shape factor calculated from the dimensions of the block – in this case it is defined as [15],

$$S = \frac{lw}{2t(l + w)}$$

<div align="right">**Equation 8**</div>

Rearranging Equation 5 for d_c and substituting in Equations 6-8, gives Equation 9.

$$d_c = \frac{F_c t}{lwE_0\left(1 + \psi\left(\frac{lw}{2t(l + w)}\right)^2\right)}$$

<div align="right">**Equation 9**</div>

For the block analysis: $F_c = 24$ N, $E_0 = 7.33 \times 10^6$ Pa, $\psi = 2.23$ [17], $l = 0.006$ m and $w = 0.006$ m. Setting $t = 0.003$ m and using Equation 9 gives the d_c value for the bonded case. Alternatively, setting $t = 0.006$ m and then only taking half the deflection from Equation 9 gives the sliding condition due to symmetry as shown in Figure 5.
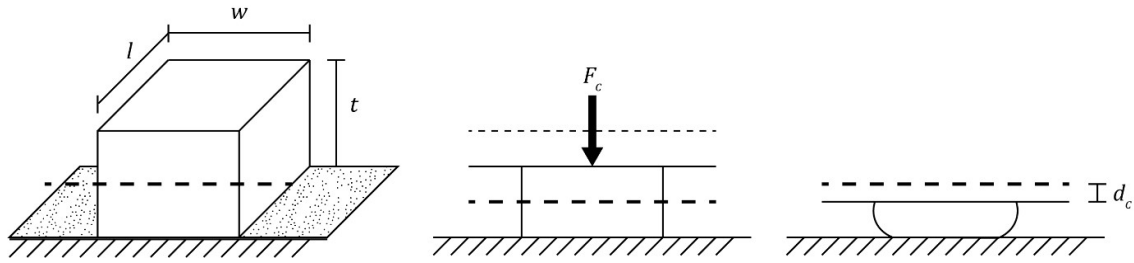
**Figure 5. Diagram showing some of the parameters for Equations 5 – 9.**

Results for d_c values obtained through analytical and FE approaches are summarised in Figure 6. It can be seen that as friction increases, the compression reduces. One might expect that the FE results would lie between the analytical bonded and sliding conditions – however, in Figure 6 it can be seen that the FE shows slightly smaller deformation. As similar differences have been noted elsewhere [18], the FE model compression is judged adequate.
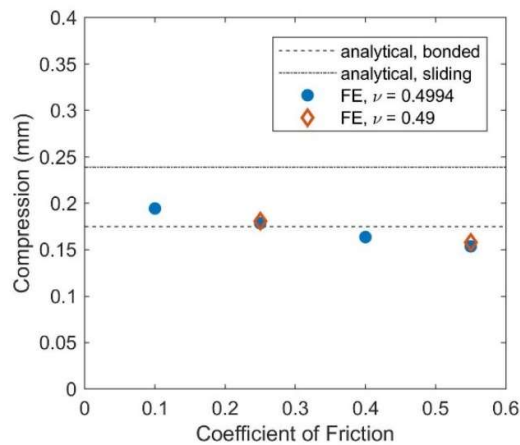
**Figure 6. Compression of the rubber block obtained using different approaches**

2.3.2 Slide behaviour

Results showing the sensitivity to compressibility and friction coefficient during the sliding phase are summarised in Figure 7. As mentioned earlier, it is important to note that only half the block was modelled and symmetry enforced on one surface. Hence for Figure 7, the normal force is 12 N and the original contact area is 18 mm^2.
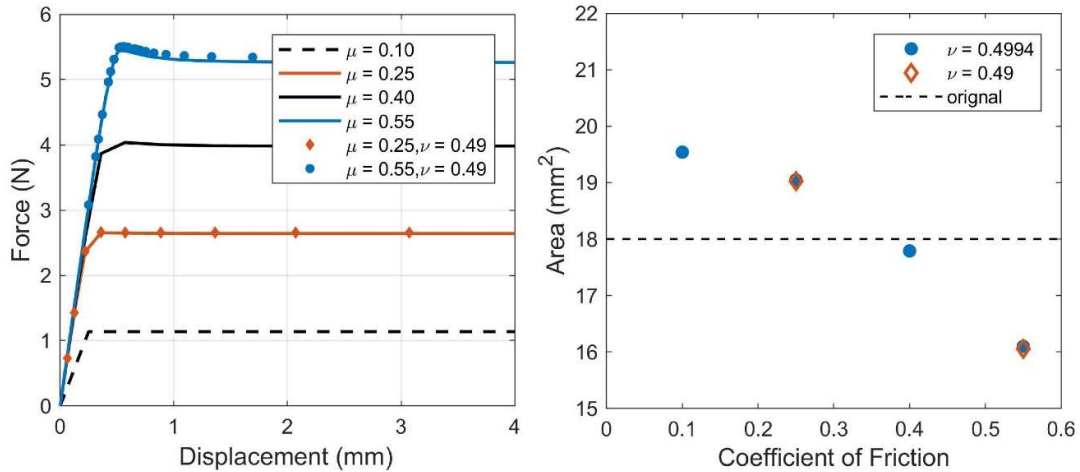
**Figure 7. Friction force-displacement and stabilised contact area for the block during sliding**

It is clear from Figure 7 that compressibility (specified using Poisson's ratio, v) is not an important factor in this type of analysis. This is a reasonable conclusion because the rubber is not highly constrained. Friction coefficient on the other hand, has a major effect on the results. It controls the extent to which the rubber spreads laterally at the contact, which in turn affects the pressure distribution and the contact area. To illustrate this, a plot showing the typical deformation and strain distribution across the block during sliding in presented in in Figure 8.
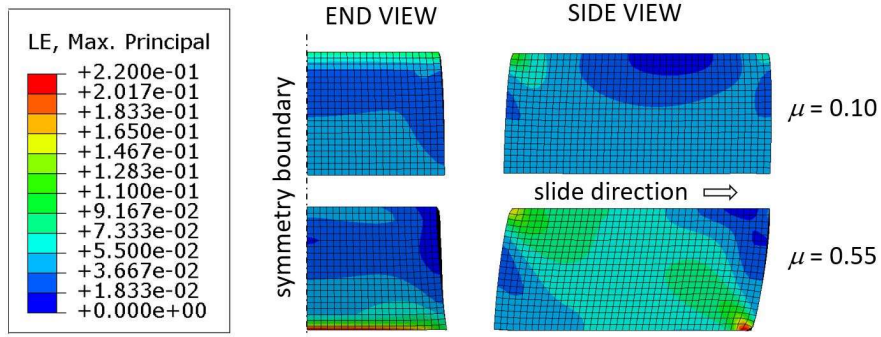
Figure 8. Deformation and strain distribution across the block model sliding for different friction coefficients.

2.3.3   Comparison between FE and Experimental

To compare simulation with a real rubber sliding scenario, an experimental test was devised. Using the set-up outlined in Figure 9, physical contact area analysis was conducted using the frustrated total internal reflection method [19] and the same UMT as that which is previously mentioned. A 6 × 6 mm rubber sample of TY-Green, was pressed in contact with a 10 mm thick Perspex sheet lined perimetrically with ultrabright LEDs. A normal load of 12 N was applied to the rubber sample before sliding at a velocity of 1 mm/s. These same loads and velocities were used during simulation for comparison. A coefficient of friction value of 0.95 was used in the simulation as this was like that observed experimentally.
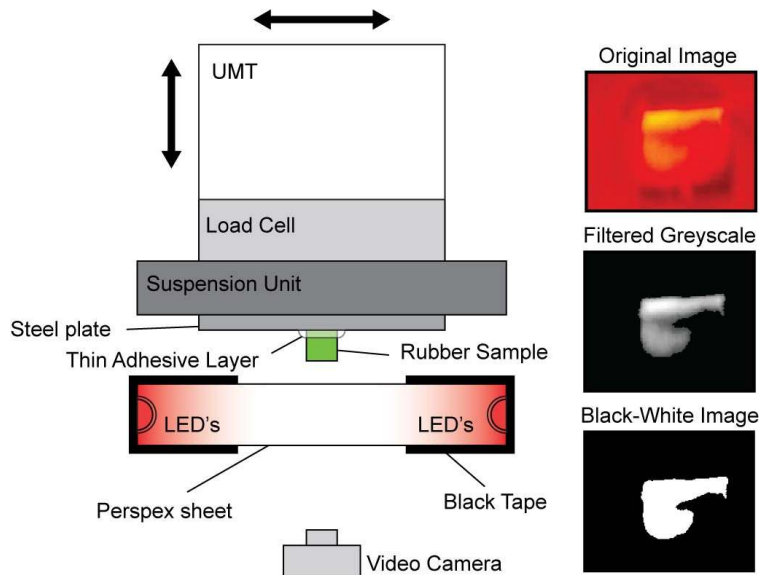

Figure 9. Schematic of contact area experiments. The images on the right show an example of how the areas of contact are separated from the background.

Using Python 3, the bright areas of each frame (recorded at 30 Hz), which indicate the areas of contact between the rubber and the surface, were identified and their pixel count recorded. As such, contact area percentage was measured for the slide and compared to that observed during simulation. This plot is shown in Figure 10 along with the force-time graphs. The force-time trace was measured using the loadcell affixed to the UMT and recorded at 125 Hz.

Similarities between simulation and experiment include the general contact area and friction force trace shapes and the transient drop in contact area that occurs at 0.9 s. The primary discrepancy can be observed from 1.5 s onward on the contact area trace. Experimentally, contact area was seen to steadily increase during sliding, whereas the simulation remained constant. This increase in contact area is thought to be a result of the internal softening of the rubber over time in combination with slight misalignments in the experimental set-up.

The misalignment of the rubber block meant that over time the internal relaxation of the rubber increased the contact area at a greater rate than if it sat perfectly flat due to the higher local pressures experienced.
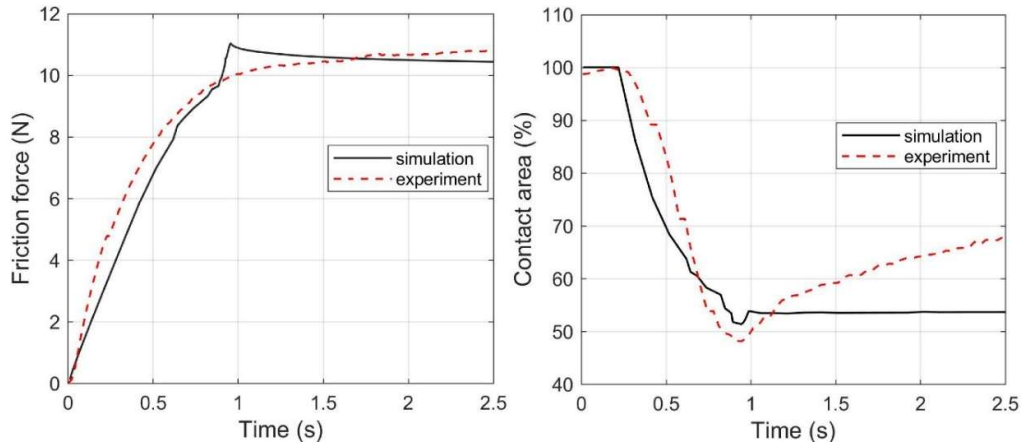
Figure 10. Force and Contact area against time graphs for the FE model and experiment.

2.4 Development of the tread segment model

The tread segment model, shown in Figure 11, was a refinement of the block model with more representative geometry and improved meshing. The important differences in terms of geometry are the reduction in area near the contact surface (accommodating the tread grooves) and 0.1 mm radii on the edges at the contact surface. The analysis of the block revealed that while most of the block experiences relatively gradual deformation gradients, there are hot spots in the contact area, particularly around the leading edge when the friction is high. As a result, the mesh density was increased significantly around the hot-spots.
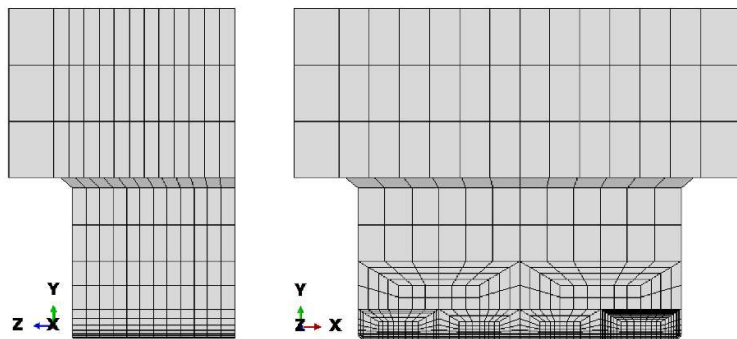
Figure 11. The single tread segment model. The mesh is concentrated at the leading edge.

A mesh convergence study was conducted considering von-Mises Stress and y-displacement. The von-Mises Stress converged at around 9000 nodes and y-displacement

converged at around 7500. Consequently, the mesh shown in Figure 11 with 9500 nodes was regarded as adequate.

In a real slip resistant shoe, the top face of the tread element would be attached to a much stiffer midsole. Therefore, in the FE simulation a beam multi-point constraint was applied to the top face so that the nodes on this face experience equal displacement during sliding. Rotation of this face was set to zero but vertical displacement was allowed. Finally, a 30 mm/s slide velocity was also applied to this face, with direction parallel to the contact surface.

3. Numerical simulation results

The tread segment models were used in simulation studies. For these analyses, the Poisson's ratio was reduced to 0.49. While this results in an unrealistically low bulk modulus for the material, it enabled the use of standard rather than hybrid elements which avoided problems with analysis convergence when considering viscoelastic material behaviour. It was shown in a previous section that compressibility does not affect the results significantly in these analyses.

3.1 Viscoelasticity and loading rate

The effects of viscoelasticity on the behaviour were evaluated by investigating the effects of three different velocities for horizontal motion. These were compared with two quasi-static analyses carried out using purely elastic properties. Results are presented in Figure 12 and again based on the half-model with the total compressive load of 12 N and nominal contact area of 18 mm^2.
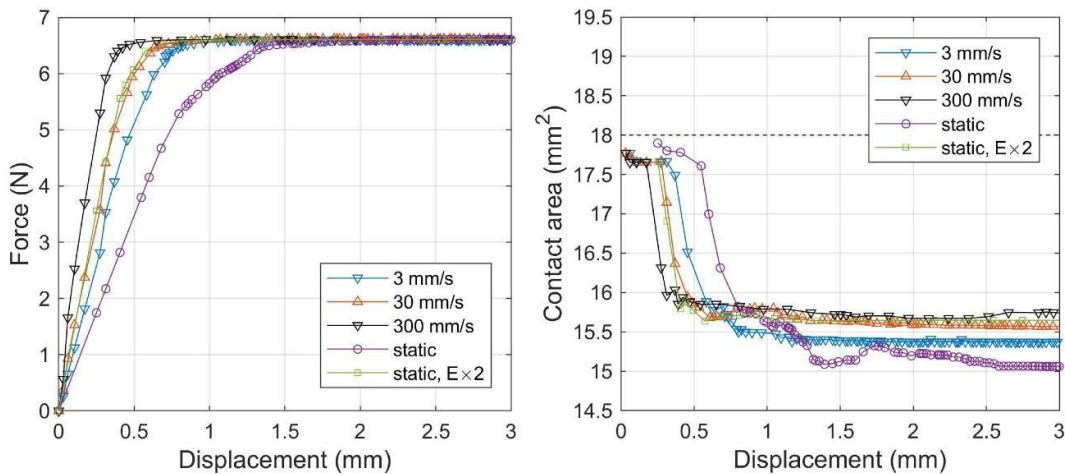

Figure 12. Friction force (left) and contact area (right) graphs during sliding of models at different speeds with and without viscoelastic material properties.

It can be seen that the dynamic 30 mm/s loading curves are matched almost identically by curves for static analysis with an elevated single value of modulus (E×2=14.66 MPa) which is approximately the value of the relaxation modulus (Figure 3) over the time duration in question. The results therefore suggest that there is very little difference between incorporating viscoelastic behaviour and simply using an elastic modulus that is suitably increased to match the value of the relaxation modulus over the duration of interest. Note that slower loading appears to delay the onset of slip as shearing takes place in the material. However, once slipping starts, the area reduction for the softer material (or lower loading rate) is the greatest. Note that results for the compression stage are not shown as they were all applied over the same time (0.1 s) so only the static loading case was different.

3.2 Effect of Tread

The FE model geometry was modified by adding a second tread element and applying double the normal load applied to a single tread element. These results were then mirrored to imitate the real tread pattern (Figure 13).
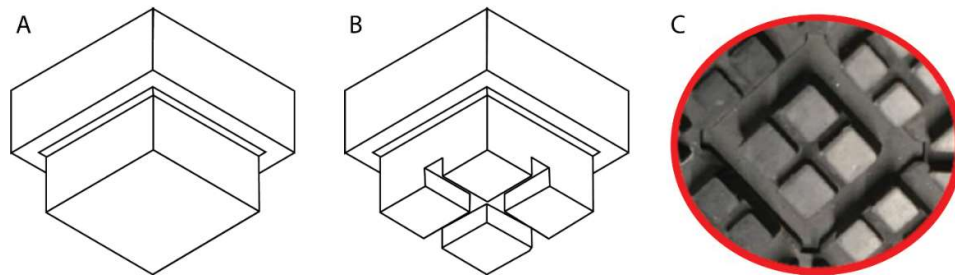
Figure 13. Single block design (A) and the realistic tread design (B) shown in comparison to the real tread pattern (C).

The effect of tread was then evaluated through comparison of a single block with the new, representative, treaded design. Figure 14 shows the realistic geometry overlaid on the single block as both are sliding, and Figure 15 compares contact pressures of the two designs.
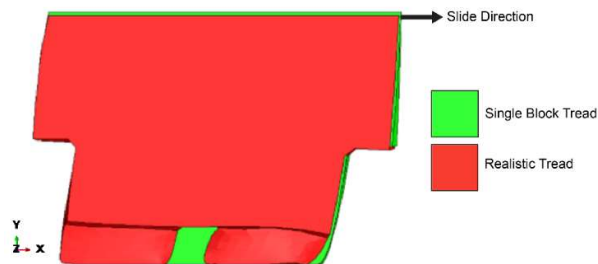
Figure 14. The lateral view of the sliding single block and realistic tread designs.

The ratio of sliding contact area and the nominal contact area was calculated for the single tread element and the realistic geometry. The single tread element maintained a higher contact area ratio during sliding in comparison to the realistic geometry, with ratios of 0.84 and 0.71 respectively. The contact pressure concentration at the rubber block's leading edge, the removal of contact at the rear of the block and the slight squeezing observed on the lateral sides are all characteristic features of sliding rubber and have also been observed experimentally.
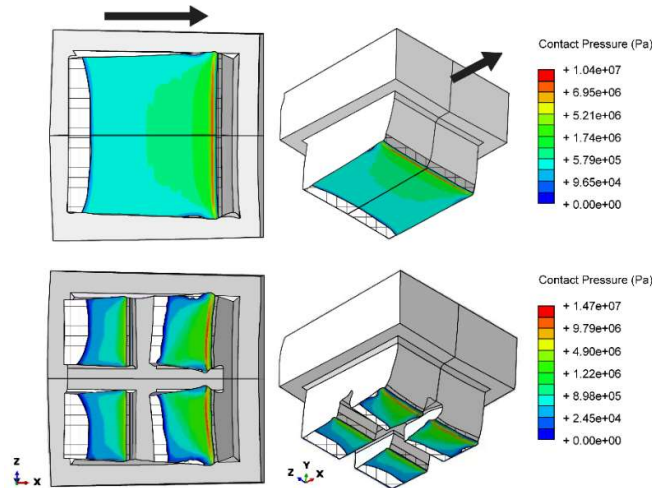
Figure 15. FE contact pressure distributions of a single tread block (top) and the realistic tread design (bottom) during sliding. Two orientations of both models are shown. Respective slide directions are shown on the single block model with crosshatch showing areas of zero contact.

The von-Mises stress distributions across the entire FE models are shown in Figure 16. As can be seen, max stress occurs at the front edges for both designs. However, the realistic tread has a second area of stress concentration on the leading edge of the trailing elements. The max von-Mises stress values were recorded as 8.49 MPa for the realistic tread geometry and 7.44 MPa for the single tread element geometry.
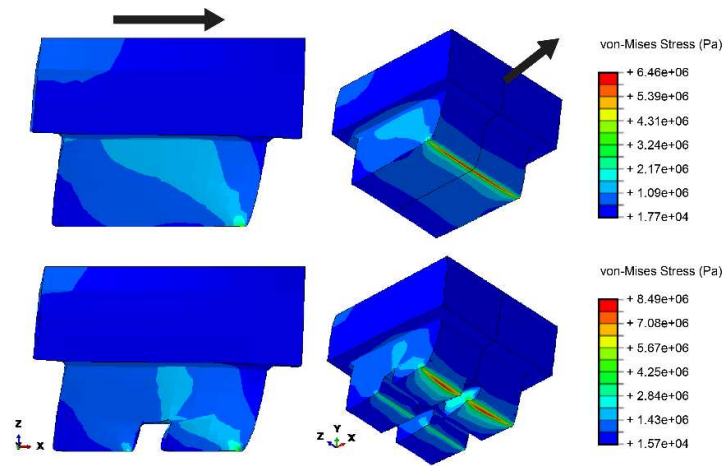
Figure 16. FE von-Mises stress distributions of a single tread block (top) and realistic tread design (bottom) during sliding. Two orientations of both models are shown. Respective slide directions are shown on the single block model.

4. Discussion

Initial analyses using the simple block showed that the models provided reasonable representation of the compression behaviour and that material compressibility is not a major concern. However, the deformed shape during sliding is affected considerably by the friction coefficient. It was also shown that the FE model replicates aspects of experimental rubber sliding in terms of friction force generation and contact area reduction during the initiation of sliding. The most noticeable difference between simulation and experiment was observed in the contact area plots. Experimentally, during steady sliding, contact area steadily increased. Conversely, the simulation reported a constant contact area during sliding. This is thought to be the result of strain softening in combination with slight a misalignment of the rubber block with the Perspex surface.

The FE model shows a loss of rubber-surface contact at its rear, as the tread element undergoes bending caused by the frictional force, also known as friction-induced torque [20]. This same lifting at the rear of sliding rubber tread elements has been recorded in other FEM studies [12,21] and experiments alike [20–23] as has the pressure concentration and deformation observed at the FE model's leading edge. Therefore, though discrepancies are present in the recorded contact areas during steady sliding, it is considered that the FE model sufficiently replicates the initial slip conditions of rubber along with the characteristic leading edge, lateral squeezing and lifting of the rear.

When comparing the deformation characteristics of the simplified model with the realistic tread pattern (Figure 14), the inclusion of the cross cut-out groove results in greater

deformation, both in terms of general compression and of the individual tread elements. This is due to the reduction of material, while maintaining the square section, reducing the stiffness of the individual elements. Furthermore, the contact area is also reduced by an additional 13% in comparison to the single tread block, due to this increased flexing of the tread elements. This reduced contact area consequently engenders an increased max contact pressure from 10.4 MPa to 14.7 MPa. This increase in max contact pressure occurs at the front edges and suggests that the realistic tread pattern will wear at a greater rate than on the single block. On dry surfaces, increased wear has been linked to increased friction [24,25]. However, worn down front edges are likely to decrease the shoe surface friction on wet surfaces through a reduction of groove depth. Additionally, chamfering of the front edge will weaken the fluid wiping capabilities of the tread.

In Figure 15, the leading edge of the realistic tread model is shown to slant inwardly, creating an oblique frontal edge. Blanchett and Powers state that oblique tread is beneficial to increasing μ_k as it provides both resistance to motion and fluid dispersion [9]. So, whereas the simple block model will provide a greater resistance to motion, due to its stiffer structure and lesser frontal deformation, it has no method for fluid dispersion which is crucial for slip resistant footwear.

The effects of frictional heating and the acknowledgment of any occurring non-linear viscoelasticity are both factors that would improve the FE model. As would the inclusion of lubricant and surface roughness, though these additions will drastically increase the complexity and computational run-time of the simulation. Other improvements of the FE model in representing a real heel-foot strike are limited by its replication of the forces and motion defined by BS EN ISO 13287:2012. This standard breaks the step into two distinct stages: loading and sliding. In a regular gait, shoe slides are consequent of a single, angular loading scenario. Loading the tread patterns in a way that is more characteristic of real heel-strikes may identify more important aspects of tread design when considering slip resistance.

5. Conclusions

A real tread design from a slip resistant shoe has been modelled and simulated under the conditions of a slip resistance standard for footwear. The models have been used to show that material compressibility is not a significant factor in the deformation of the tread under compression and sliding. It can also be shown that the effects of viscoelasticity can be approximated by a purely elastic model with a single, appropriately selected value of modulus for a range of loading rates. The friction coefficient between the tread and the ground have a significant effect on the shape that the contact surface takes. Higher friction

and softer materials result in the development of a high stress zone near the leading edge and a loss of contact at the trailing edge. Discussion was then provided as to the fluid dispersion and wiping implications of different tread patterns. The adding of tread grooves to a rubber block has shown a decrease in the ratio of sliding to nominal contact area and a change in the stress distribution within the block. The inclusion of grooves also resulted in a difference in leading edge characteristics, from flat to oblique, made by the addition of a central groove.

The FEM described in this paper can be applied to other, more complex tread patterns such as herringbone and concentric, although additional computational cost is to be expected along with a more difficult meshing procedure.

Further validation of the results should also be attempted by extending the experimental work to different material types, applied loads and friction coefficients.

Acknowledgements

References

[1]   Health and Safety Executive. Kinds of accident in Great Britain , 2013 2019:1–9.

[2]   Verma SK, Chang WR, Courtney TK, Lombardi DA, Huang YH, Brennan MJ, et al. A prospective study of floor surface, shoes, floor cleaning and slipping in US limited-service restaurant workers. Occup Environ Med 2011. doi:10.1136/oem.2010.056218.

[3]   Beschorner KE, Albert DL, Redfern MS. Required coefficient of friction during level walking is predictive of slipping. Gait Posture 2016;48. doi:10.1016/j.gaitpost.2016.06.003.

[4]   Li KW, Chen CJ. The effect of shoe soling tread groove width on the coefficient of friction with different sole materials, floors, and contaminants. Appl Ergon 2004. doi:10.1016/j.apergo.2004.06.010.

[5]   Li KW, Chin JC. Effects of tread groove orientation and width of the footwear pads on measured friction coefficients. Saf. Sci., 2005. doi:10.1016/j.ssci.2005.08.006.

[6]   Li KW, Wu HH, Lin YC. The effect of shoe sole tread groove depth on the friction coefficient with different tread groove widths, floors and contaminants. Appl Ergon

2006. doi:10.1016/j.apergo.2005.11.007.

[7]   Tsai HK, Li KW, Chen CC. Effects of footwear sample area on the friction coefficient on the floor. IEEE Int. Conf. Ind. Eng. Eng. Manag., 2016. doi:10.1109/IEEM.2015.7385664.

[8]   Shaghayegh Bagheri Z, Anwer A, Fernie G, Naguib HE, Dutta T. Effects of multi-functional surface-texturing on the ice friction and abrasion characteristics of hybrid composite materials for footwear. Wear 2019;418–419. doi:10.1016/j.wear.2018.11.030.

[9]   Blanchette MG, Powers CM. The influence of footwear tread groove parameters on available friction. Appl Ergon 2015. doi:10.1016/j.apergo.2015.03.018.

[10]   Singh G, Hasija V, Menezes PL, Beschorner K. Using a 3-Dimensional viscoelastic finite element model to analyze the effects of floor roughness, sliding speed and material properties on shoe-floor friction. Am Soc Mech Eng Tribol Div TRIB 2012:255–7. doi:10.1115/IJTC2012-61176.

[11]   Wagner P, Wriggers P, Klapproth C, Prange C, Wies B. Multiscale FEM approach for hysteresis friction of rubber on rough surfaces. Comput Methods Appl Mech Eng 2015. doi:10.1016/j.cma.2015.08.003.

[12]   Hofstetter K, Grohs C, Eberhardsteiner J, Mang HA. Sliding behaviour of simplified tire tread patterns investigated by means of FEM. Comput Struct 2006. doi:10.1016/j.compstruc.2006.01.010.

[13]   Wei C, Olatunbosun OA. Transient dynamic behaviour of finite element tire traversing obstacles with different heights. J Terramechanics 2014. doi:10.1016/j.jterra.2014.07.001.

[14]   Wang J, Sun D, Liu S, Zhang X. Damping Characteristics of Viscoelastic Damping Structure under Coupled Condition. Math Comput Appl 2017. doi:10.3390/mca22010027.

[15]   Pritz T. Unbounded complex modulus of viscoelastic materials and the Kramers-Kronig relations. J Sound Vib 2005. doi:10.1016/j.jsv.2003.11.040.

[16]   Lakes RS, Wineman A. On poisson's ratio in linearly viscoelastic solids. J Elast 2006. doi:10.1007/s10659-006-9070-4.

[17]   Sheridan PM, James FO, Miller TS. Engineering with Rubber. Pennsylvania, USA: CARL HANSER VERLAG; 1992.

[18]   Hill JM, Lee AI. Large elastic compression of finite rectangular blocks of rubber. Q J Mech Appl Math 1989. doi:10.1093/qjmam/42.2.267.

[19]   Needham JA, Sharp JS. Watch your step! A frustrated total internal reflection approach to forensic footwear imaging. Sci Rep 2016;6:1–7. doi:10.1038/srep21290.

[20]   Maegawa S, Itoigawa F, Nakamura T. A role of friction-induced torque in sliding friction of rubber materials. Tribiology Int 2016;93:182–9. doi:10.1016/j.triboint.2015.08.030.

[21]   Tuononen AJ. Onset of frictional sliding of rubber-glass contact under dry and lubricated conditions. Sci Rep 2016;6. doi:10.1038/srep27951.

[22]   Maegawa S, Itoigawa F, Nakamura T. Effect of surface grooves on kinetic friction of a rubber slider. Tribol Int 2016;102. doi:10.1016/j.triboint.2016.05.019.

[23]   Moriyasu K, Nishiwaki T, Shibata K, Yamaguchi T, Hokkirigawa K. Friction control of a resin foam/rubber laminated block material. Tribol Int 2019;136:548–55. doi:10.1016/j.triboint.2019.04.024.

[24]   Hale J, Lewis R, Carré MJ. Rubber friction and the effect of shape. Tribol Int 2020. doi:10.1016/j.triboint.2019.105911.

[25]   Emami A, Khaleghian S. Investigation of tribological behavior of Styrene-Butadiene Rubber compound on asphalt-like surfaces. Tribol Int 2019;136:487–95. doi:10.1016/j.triboint.2019.04.002.